Morphological Entanglement in Living Systems

Thomas C. Day[1], **S. Alireza Zamani-Dahaj**[1], **G. Ozan Bozdag**[2], **Anthony J. Burnetti**[2], **Emma P. Bingham**[1], **Peter L. Conlin**[2], **William C. Ratcliff**[2], **Peter J. Yunker**[1]

[1]School of Physics, Georgia Institute of Technology

[2]School of Biological Sciences, Georgia Institute of Technology

Abstract

Many organisms exhibit branching morphologies that twist around each other and become entangled. Entanglement occurs when different objects interlock with each other, creating complex and often irreversible configurations. This physical phenomenon is well studied in nonliving materials, such as granular matter, polymers, and wires, where it has been shown that entanglement is highly sensitive to the geometry of the component parts. However, entanglement is not yet well understood in living systems, despite its presence in many organisms. In fact, recent work has shown that entanglement can evolve rapidly and play a crucial role in the evolution of tough, macroscopic multicellular groups. Here, through a combination of experiments, simulations, and numerical analyses, we show that growth generically facilitates entanglement for a broad range of geometries. We find that experimentally grown entangled branches can be difficult or even impossible to disassemble through translation and rotation of rigid components, suggesting that there are many configurations of branches that growth can access that agitation cannot. We use simulations to show that branching trees readily grow into entangled configurations. In contrast to nongrowing entangled materials, these trees entangle for a broad range of branch geometries. We, thus, propose that entanglement via growth is largely insensitive to the geometry of branched trees but, instead, depends sensitively on timescales, ultimately achieving an entangled state once sufficient growth has occurred. We test this hypothesis in experiments with snowflake yeast, a model system of undifferentiated, branched multicellularity, showing that lengthening the time of growth leads to entanglement and that entanglement via growth can occur for a wide range of geometries. Taken together, our work demonstrates that entanglement is more readily achieved in living systems than in their nonliving counterparts, providing a widely accessible and powerful mechanism for the evolution of novel biological material properties.

I. INTRODUCTION

Many organisms grow with filamentous, branching morphologies, including plants, mycelial networks, cyanobacterial mats, and more. These branched treelike organisms often wind around themselves or others, thus becoming visually tangled (Fig. 1). This physical phenomenon, called "entanglement," is well studied in nonliving materials [1–10], where it is known to fundamentally affect material properties (e.g., rheological properties of polymer melts [11–15]). Entanglement has also recently become a topic of interest in active systems [16–18]. Entanglement provides these systems unique and potentially useful

material properties. For instance, materials composed of entangled components are generally both strong and tough [6,8] and exhibit strain stiffening [3]. But, these studies also make it clear that entanglement requires either precise engineering of the structure (for example, entangled polymers often require chemical cross-linking [4,6–8]) or precise geometry of the entangling constituents [2,3]. However, the growth of an organism is qualitatively distinct from the assembly of nonliving materials. Entangled multicellular systems experience birth and death events, providing sink and source terms to their continuity equation [19], their branches consist of many cells, making them effectively athermal, and they are also evolved rather than designed. Therefore, the rules for generating nongrowing entangled materials do not necessarily apply to entanglement via growth, leaving it unclear what determines whether growing systems do or do not entangle.

It was recently discovered that entanglement rapidly evolves, *de novo*, in multicellular yeast clusters [23]. These clusters, known as "snowflake yeast," initially grow as branched trees. They are subjected to selection for large size every day for 600 days; over this time, snowflake yeast evolves a new morphology in which disconnected branches are physically entangled, enabling clusters to grow larger than 1 mm in size. The speed and ease with which snowflake yeast evolves entanglement, combined with the presence of many entangled organisms in nature (Fig. 1), suggests either that all of these organisms are coincidentally positioned near a specific structural and geometric entanglement sweet spot or that there is a broader physical principle that enables entanglement via growth for a wide range of growing branched trees.

Here, we use a combination of experiments and a variety of numerical modeling methods to show that growth readily establishes entanglement in branched trees for nearly any geometry, unlike entanglement of nongrowing elements. We find that these entangled configurations are difficult or even impossible to access through translation and rotation alone; in other words, the structures produced by growing, entangled branches cannot be assembled like rigid, granular, nonliving materials. First, we use numerical manipulations of experimental data to interrogate what kinds of entangled branches can or cannot be disassembled. Then, we develop a simple simulation to investigate how entangled configurations of branches arise and how entanglement probability is affected by geometric properties of the branches. Surprisingly, we find that entanglement via growth is generically easy to achieve, almost regardless of branch geometry. This leads us to develop a simple model, without specifying a growth morphology, to explore the onset of entanglement via growth. We find that entanglement can be a slow process, suggesting that, for growing branched trees, entanglement depends primarily on timescales—if growth does or does not stop before entanglement is complete—rather than geometry. We test this idea in experiments by growing branching microbes, explicitly manipulating the length of time they sit next to one another, and separately their branching geometry, confirming that timescales control entanglement via growth.

II. ENTANGLED, GROWING BRANCHES

We begin by investigating an experimental system that is known to grow into entangled configurations, a multicellular baker's yeast called snowflake yeast [23]. Snowflake yeast

form structures that resemble branching trees via continued rounds of cell division. New cells bud from their mother cell and remain attached through a rigid chitinous bond; if the bond breaks, it is not reformable. Cells do not adhere via sticky interactions such as surface flocculation proteins or extracellular matrix. Therefore, cells are connected one to another in a treelike pattern, such that breaking any chitinous bond breaks the group into two pieces [24–26]. We use snowflake yeast strains taken from an ongoing long-term evolution experiment [23]. We have previously found that branches of yeast cells can interact sterically with one another, intercalating and entangling within a single yeast tree [23], with entanglement arising *de novo* in fewer than 600 days of experimental evolution. Given the precision necessary to create nonliving entangled materials, it is surprising that this new morphology evolves so readily in all five independently evolving populations. This observation suggests that perhaps entanglement via growth is fundamentally different than entanglement of nonliving materials.

We first test if agitation affects the integrity of entangled branches. Unlike previous experiments with entangled granular materials, in which mechanical agitation leads to collapse of a rigid column [2], or in observations of active tangled matter, which can reversibly tangle and untangle quickly [18], the snowflake yeast branches appear difficult, if not impossible, to disassemble. When vortex mixed at medium strength, snowflake yeast groups maintain their size distribution, suggesting that mechanical agitation (weak enough to not break intercellular bonds) alone cannot disassemble the tangled aggregate [Fig. 2(a)]. Crucially, although there are mathematical tools to rigorously measure the entanglement complexity of open curves in three dimensions [27,28], there is yet no rigorous method to predict if such configurations are geometrically trapped. We, therefore, turn to empirical tests of snowflake yeast at the microscale to confirm if growth accesses configurations that cannot be disassembled.

Previous work used scanning electron microscopy to image 3D volumes of a single snowflake yeast group [23]. Here, we segment each disconnected branch of cells in those 3D image stacks and generate 3D surface data by approximating their surfaces through alpha shapes [Fig. 2(b)]. We then seek to measure the degree of entanglement of these surfaces. While there are elegant methods for computing the degree of entanglement, including contour reduction algorithms and the average crossing number [29,30], applying these methods to branched structures is nontrivial. We instead employ a brute-force method by computationally simulating artificial translations and rotations of various branches of cells and tracking their collisions (see Appendix D). Using this method, we investigate if the experimentally observed configurations that snowflake yeast grow into can be disassembled via mechanical agitation.

We quantify the degree of confinement by performing simulations in which we translate one yeast branch with respect to others. We identify two separate branches [Fig. 2(b)(i)] that are entangled, where entanglement is defined as occurring when one disconnected branch penetrates the convex hull of another, a definition broadly used when studying entanglement [2,3,23]. We construct alpha shapes of both pieces. Then, we translate the two alpha shapes with respect to each other by identifying one target piece [the gray piece in Fig. 2(b)] and one stationary piece and moving the target piece a distance of 1.3 cell lengths in

discrete steps of size 0.03 cell lengths. We allow the alpha shapes to overlap and at each step measure the overlapping volume between the two alpha shapes. We repeat this "drag experiment" 1000 times in different directions, each direction defined by a unit direction vector, each vector evenly dispersed around the unit sphere. Contact is defined to be the point at which the overlapping volume exceeds one cubic micron (see Appendix D). Of the 1000 sampled directions, 35 do not make contact exceeding this threshold, indicating that the two pieces are not prohibitively entangled. The median first contact distance is 0.20 cell lengths [Fig. 2(c)]. We next add a third branch of cells from the same snowflake yeast cluster [Fig. 2(b)(ii)] and repeat the drag simulation. With three branches, contact occurs in every translation direction, and the median first contact distance is 0.13 cell lengths. Thus, in this example, the entangled piece can sometimes escape one neighbor, but it cannot escape two neighbors.

While these simulations suggest that these three branches are highly entangled, it is possible that the target branch can escape with a simple series of translations and rotations— maneuvers that are readily accessible to nonliving materials. To test this idea, we randomly translate and rotate the branches to determine if they can undo snowflake yeast entanglement from growth. In our algorithm, one branch (the target) experiences movements that combine a random translation (a step of 0.4 μm, or approximately 0.03 cell lengths, in a random direction) and a random rotation (a rotation of 2° around a randomly selected axis). Collisions are identified by tracking the overlapping volume of the target branch with other branches. Random movements are accepted if the branches do not collide and rejected if they do collide, in which case the target piece remains at its last non-overlapping position and orientation. From our drag experiments, we hypothesize that our target branch could be disassembled if it interacted with only one other branch but may be confined when interacting with two or more others. To explore how many branches are required for confinement with these specific geometries, we simulate several different configurations of branches with varying numbers of interacting pieces.

Following this procedure, we first agitate the target branch [gray, Fig. 2(b)(i)] in free space, tracking the position of its center of mass and calculating its mean squared displacement (MSD, $\langle [x(t + \tau) - x(t)]^2 \rangle$) over 100 simulations, each running for 3000 time steps [Fig. 2(d)]. The unconfined branch moves diffusively with diffusion constant $D_0 = 9.77 \times 10^{-4} \pm 1 \times 10^{-6}$ cell lengths squared per simulated time step. Next, we simulate a pair of interacting branches [Fig. 2(b)(i)] and run 100 replicate simulations. We use the same target branch (gray) as for the freely diffusing case. We find that the target branch still moves diffusively, which is consistent with our previous observation that the two-piece interaction is escapable. However, the effective diffusion constant is lower ($0.33 D_0 = 3.21 \times 10^{-4} \pm 1 \times 10^{-6}$ cell lengths squared per unit time) due to the many collisions between the two pieces. Upon adding a third disconnected branch [Fig. 2(b)(ii)], we find that the MSD of the target piece ceases to grow linearly, indicating that it is caged by its neighbors, even when the simulation run-time is extended to be an order of magnitude longer than the other simulations. Upon adding all remaining pieces [Fig. 2(b)(iii)], motion is even more limited. To quantify this caging effect, we measure an effective diffusion constant for all four scenarios with the gray target piece, scaled by the free-space diffusion constant, and find that D_{eff} approaches zero for three- and four-branch simulations [Fig. 2(e), top]. Further supporting the caging

observations, we find that the fraction of agitation simulations for which the target piece moves at least one cell length scales with the effective diffusion constant [Fig. 2(e), bottom, Pearson correlation coefficient $r = 0.86$].

To test if other branches in the cluster behave similarly, we repeat this agitation experiment with an entirely different set of branches [Fig. 2(b)(iii)]. In this example, we agitate the yellow branch with zero interactions, one interacting branch (pink), two interacting branches (pink and green), and three interacting branches (pink, green, and black). In Fig. 7, we report the same characteristic flattening of the mean squared displacement upon adding the second interaction and include measurements of the effective diffusion constants. Last, as a demonstration for just how dramatic this caging effect can be, we agitate one branch that is entangled with 16 others [pink, Fig. 2(b)(iii)]. After 50 replicate simulations, each with 3000 time steps, the agitation algorithm is never successful in completing even a single accepted move (i.e., one that results in zero collisions).

The above results suggest that branches entangled with two or more other branches grew into highly confined configurations that would be very difficult, if not impossible, to reach through translations and rotations. We, thus, next seek to determine how many branches are entangled with two or more other branches within macroscopic clusters. To do so, we identify 38 discrete branches and compute the convex hull of each one. Then, for each component, we determine how many other convex hulls it penetrates, i.e., its coordination number z [Fig. 2(f)]. We find that all branches penetrate the convex hull of at least one other branch and 92% of the branches penetrate the convex hulls of two or more other pieces. The average coordination number is $\langle z \rangle = 4.2 \pm 2.7$. Therefore, snowflake yeast branches appear to be highly confined.

These analyses of entangled branches suggest that entanglement via growth can achieve configurations that are difficult, if not impossible, to disassemble via translation and rotation alone. In those configurations, the only way to disassemble two or more entangled branches appears to be to destroy or deform the material, for example, through external forces that rupture cell-cell bonds or via branch death. However, it is unclear if snowflake yeast coincidentally possess a growth morphology with a geometry conducive to such highly confined, entangled branches, or if entanglement via growth is readily able to access such configurations. To answer this question, we seek to explore entanglement through growth via a model system that grows with a branched morphology and a tunable geometry.

III. ENTANGLEMENT FROM GROWTH VIA RIGID-BODY SIMULATIONS

To test if entanglement is, in general, readily achieved via growth, we simulate growing, branching trees in three dimensions with a variety of geometries. We vary the geometry of these growing trees and determine which geometries do and do not allow entanglement to occur. Our simulations start with six "primary" tips, centered at the origin, with each tip pointed along one of the cardinal axes. Tips have a fixed diameter d and grow by continually lengthening at a constant rate. After lengthening by a distance Λd, each tip branches into two tips. The two new tips branch symmetrically from the growth axis prior to splitting, with branching angle θ and random azimuthal orientation ϕ [Fig. 3(a)]. If a growing branch

collides with a branch on another tree that is already present, the growth is rejected and the branch "retreats" by a small amount, 0.02Λ; then, it deflects by turning in a random orthogonal direction. It then proceeds to lengthen and branch with its new orientation, which could result in more collisions that are similarly deflected. The lengthening and branching processes are repeated to form a highly branched tree; in principle, lengthening and branching could repeat indefinitely, but here the simulation is truncated after a set number of branching events per tree (B), which could be different for each tree. Control parameters Λ and θ allow us to test a wide variety of branch geometries.

The goal of these simulations is to investigate the range of geometries that facilitate entanglement via growth. As such, we employ no other mechano- or chemosensing behavior; we also do not allow the dendrimers to elastically deform. Any of those behaviors would make entanglement more likely to occur, so we exclude them to keep the focus on geometry. Thus, these simulations can be considered simple random walk models of dendrimerlike growth that investigate the geometries of growing and entangling branches. We also simulate an alternative approach in which we make entanglement even more difficult to achieve; growing tips that collide with existing branches cease growing; these simulations produce results qualitatively similar to what we detail below (see Fig. 10).

A. Growth assembles configurations that mechanical agitation cannot

We next seek to assess how easily growth entangles trees compared to sequences of translations and rotations. Particularly, we hypothesize that two already-grown and nonentangled trees would have a limit to how close they can be pushed together via translations and rotations. Conversely, we hypothesize that growth could allow branches to penetrate deeper into already-grown trees, resulting in configurations that are irreversible to translations and rotations. To identify these configurations, we measure the proximity of the tree centers of mass after translating and rotating trees together and after growing trees near each another.

First, we explore how we might assemble an entangled configuration via a combination of translations and rotations. We adapt the mechanical agitation algorithm that we use to study disassembly in Fig. 2 for this purpose, with the addition that trees are periodically forced together. We grow two trees independently (geometric parameters $\Lambda = 4$, $\theta = 45°$, and $B = 4$) and translate one tree toward the other until the branches of the trees collide, as detected by any nonzero intersection of their alpha shapes [Fig. 3(b)]. After this initial collision, one tree goes through a series of small rotations and translations that are mechanically restricted through collision detection. Then, the trees are again pushed together. This process of pushing and agitating is cycled many times. We track the distance between the clusters' centers of mass over time (Fig. 11), finding that this amount of agitation leads to a plateau in the closest distance the clusters could reach by the 25th cycle. In Fig. 3(d), we plot the histogram of shortest distances achieved by the two clusters. The mean distance achieved is $L_0 = 96.1 \pm 8.8$ simulation units ($N = 188$); for comparison, the mean tree diameter is 107.9 ± 0.3 simulation units. Therefore, the pushing algorithm generally results in tree configurations that only weakly penetrate each other's space. We

scale all future measurements of tree proximity by the value L_0, such that the mean distance achieved for this set of simulations is of unit magnitude.

We next seek to model entanglement from growth. We grow one tree in isolation and then start growing the second tree 50 simulation units ($0.52L_0$) away from the first tree's center of mass [Fig. 3(c)]. This distance represents about half the mean distance between centers of mass achieved by the agitated trees and is also located inside the radius of the first tree. Because the new seed point is located slightly inside the radius of the first tree, we check if there is any initial overlapping volume (which would represent two cells occupying the same space) and generate a new location if there is. This approach results in 134 grown configurations ($B = 4$). The mean final center of mass separation distance is 55.2 ± 4.6 units ($0.57L_0$), substantially closer than through agitation alone ($p \ll 0.001$, $z = 8.9$, z test). The closest pair of agitated trees achieves a center of mass distance of 72.8 units ($0.76L_0$); only one out of the total 134 grown trees is farther apart than that. Furthermore, it is worth pointing out that grown trees achieve this small center of mass distance despite growing randomly in all directions, while agitated trees experience a directional force that is designed to push their centers of mass together. Thus, grown trees appear to readily achieve configurations that are inaccessible via agitation alone.

B. Growth geometry mediates time needed to entangle

One of the characteristics of entangling granular materials is that there is a geometric "sweet spot" for which entanglement probability is maximized [2]. We explore if such a geometric sweet spot also exists in our growing system. We test many different branch geometries by varying the geometric properties Λ (distance between branch points) and θ (angle of the new branches) as shown in Fig. 3(e). In each case, we simulate 100 different instances, where one tree is grown in isolation and then a second tree is grown nearby. Then, to quantify entanglement, we drag the two trees apart along the vector determined by the difference between their centers of mass and track collisions by quantifying the overlapping volume of their alpha shapes. We enumerate the proportion of instances where the two trees collide from this drag experiment. We find that, within the test parameters ranging from $\Lambda = [2, 6]$ and $\theta = [15, 90]$ and $B = 3$ branching events of growth, entanglement is more likely for sparser networks (larger Λ) and for intermediate branching angles ($\theta = 120°$) [Fig. 3(f)]. These results are consistent with previous experiments on entangled granular materials that identified a geometric sweet spot for maximum entanglement probability [2].

We then increase the amount of time the target tree grows, changing the number of branching events B. When trees are grown for a short amount of time, there is little entanglement observed, except for geometries near the sweet spot. At intermediate times, many configurations begin to entangle, but the geometric sweet spot is still easily observable. However, when grown for long enough, even geometries far from the sweet spot begin to entangle, and, since the probability of entanglement saturates at 1, these poorly entangling geometries "catch up" to well-entangling geometries. In Fig. 3(f), we demonstrate this saturation effect as a phase map with four panels, the first corresponding to $B = 3$ branching events and then $B = 4$, $B = 5$, and $B = 6$. There exist geometries that are not available for entanglement no matter the growth time; these geometries correspond to

very dense hyphal networks with no space between the branches [i.e., some seen in Fig. 3(e) and the gray region and line in Figs. 3(f) and 3(g)]. However, for all geometries for which entanglement can occur, the probability of entanglement increases monotonically with time [Fig. 3(g)]. This phenomenon suggests that, for entanglement via growth, the primary role of geometry is not to determine if entanglement occurs but to determine how much growth is necessary for entanglement to occur. In this sense, the amount of time a branched tree can grow may be more significant than its geometry in determining entanglement.

IV. GROWTH ENSURES TUNNELING TO ENTANGLED STATES

Our results so far suggest that entanglement via growth occurs readily for branched trees that are allowed to grow for a sufficient amount of time, with less dependence on their branching geometry. However, it remains possible that these clusters, and snowflake yeast, are especially "primed" for entangling via growth compared to entangling via agitation. We, thus, seek to test these ideas with an approach that provides maximal leniency for entanglement from agitation and that lacks a specific geometry.

To do so, we employ a nongeometric, space-filling model. In this model, we do not specify the growth morphology and do not model contact-based interactions between branches. Instead, we model the density of a branching structure as a spatiotemporal scalar field $\rho(\mathbf{r}, t)$. We consider a system with a radially isotropic density, reducing the system to one dimension. The only mechanical rule we impose is that a maximum packing density exists; i.e., the sum of all separate density fields representing different objects is limited by a maximum material packing density, $\Sigma_i \rho_i(\mathbf{r}) \leq \phi_{\max}$, where $0 < \phi_{\max} \leq 1$. This approach is inspired by simple, but fundamental, physics of close-packed particles and cells—namely, cells cannot overlap and, based on their geometry, have a maximum packing fraction they cannot exceed [26,31,32]. These packing "rules" apply to all real cellular systems but are also maximally permissive for entanglement via agitation—so long as the sum of two density fields remains less than $\phi_{\max}$, they can be pushed together such that they overlap. In fact, for this model, it would be possible to push two such objects directly through one another, so long as the packing density at every location remains below the maximum packing density, i.e., $\Sigma_i \rho_i(\mathbf{r}) \leq \phi_{\max}$ remains true everywhere. Clearly, for real, rigid objects, this is not possible. Thus, this model is quite lenient for agitated systems. Nonetheless, we find that growth easily and inevitably accesses entangled configurations in regimes that are inaccessible to agitation (Fig. 4).

We begin by modeling the time evolution of a growing system, modeled as a radially isotropic field. Growth can occur in the radial direction, thus increasing the radius, or it can occur in directions that are orthogonal or misaligned to the radial vector, thus increasing density in a region of space they already occupy. We model this time evolution as

$$\frac{\partial \rho_i}{\partial t} = K \rho_i \left(1 - \frac{\Sigma_j \rho_j}{\phi_s}\right) + D(r) \nabla^2 \rho_i.$$

(1)

The first term of the right-hand side models the dynamics of increasing density at occupied positions. Once there is material occupying a position $\mathbf{r}$, the density field at this point increases via growth until it reaches its maximum value ϕ_s, with rate of solidification K. This logistic term also includes information about other scalar density fields, with which $\rho_i(r)$ must interact. This other material acts as a further cap to the maximum density that ρ_i can reach. The second term in Eq. (1) models expansion, i.e., growth into previously unoccupied position $\mathbf{r}$. We model expansion with a diffusionlike second-order spatial derivative [with proportionality constant $D(r)$ that varies spatially] due to the stochastic random-walk-like nature of branching events in our simulations. Furthermore, we model the spatial variation of the effective diffusion constant as $D(r) = D_0[1 - (\Sigma_j \rho_j / \phi_{max})]$ to reflect the slowing rate of expansion when interacting with dense, porous material.

An important characteristic of living, growing materials (such as those in Fig. 1) is that they often do not grow to fill space; i.e., their grown packing fraction is less than the maximum possible [26,32]. Factors such as growth morphology or the uptake and diffusion of nutrients can limit the density to which the organism grows. In our model, we allow for this possibility by explicitly writing the maximum density achieved through the solidification process as ϕ_s, which may be less than the maximum possible density ϕ_{max}. We next numerically integrate our partial differential equation model. We consider two scenarios, representing entanglement via agitation and entanglement via growth. For each scenario, $\phi_s = 0.3$, a similar value to experimental measurements of the cellular packing density of snowflake yeast [32], and the maximum packing density is $\phi_{max} = 0.5$.

First, we separately grew two clusters [by integrating Eq. (1)] until they each reach ϕ_s in their center. We then push one cluster toward the other, which we refer to as the barrier. Eventually, the cluster reaches a position r_0 such that $\rho_1(r_0) + \rho_2(r_0) = \phi_{max}$. At this point, the cluster cannot be pushed any farther, as doing so results in $\phi(r_0) > \phi_{max}$ [Fig. 4(a)].

In the second scenario, we grow a barrier until it reaches ϕ_s in its center. We then grow a cluster starting a distance $r = 1$ away from the center of the barrier and observe that the cluster grows through the barrier. As the height of the barrier $\sigma_0 < \phi_{max}$, growth inevitably tunnels through the barrier to the other side, where it then continues to solidify, entangling the barrier in place [Fig. 4(a)]. Note that this is a deterministic system; tunneling through the barrier always happens for these chosen parameters.

Next, we seek to test the impact of the barrier's density and width on the timescale that it takes to traverse the barrier. We generate step function barriers with varied densities, from 0 to ϕ_{max}, and widths, from $w = 0$ to 0.6, to investigate the amount of growth time necessary to traverse the barrier. This traversal time (which we normalize by the total length of our numerical simulations, i.e., the total integration time) diverges as the barrier height approaches the maximum density. Conversely, traversal time does not diverge with barrier width, implying that, in principle, even a very wide barrier eventually is traversed. These results suggest a physical argument for barrier traversal. Passing through a barrier of a given density takes, on average, a particular amount of time per unit length. Increasing barrier width does not significantly change the paths through the barrier and, thus, does not change this traversal time per unit length; therefore, wider barriers take proportionally

longer than narrower ones. Conversely, when the barrier density is increased, the number of paths that traverse the barrier decreases, as dead ends are inevitably created. This leads to a nonlinear effect: At low densities, the number of paths through the barrier remains relatively unchanged, but at higher densities, the number of dead ends increases, making the search time for a path increase nonlinearly.

The gray region in Fig. 4(b) illustrates a regime where pushing the cluster all the way through the barrier is impossible, because the sum of the two density fields would together exceed ϕ_{max}. Growing fields can traverse the barrier even in this gray zone because growth can proceed without exceeding ϕ_{max}. This means that, even in the case of this model, which is quite lenient to translating fields directly through one another, growth still accesses configurations that translation cannot achieve, even if traversal times within the gray region are slow [Fig. 4(b)].

Finally, we seek to test some of these predictions via simulations of dynamic, growing hyphae in three dimensions. We use a sample cube of SEM data from snowflake yeast experiments to generate a porous barrier. The density of this block is controlled by eroding or dilating the voxels of the 3D data sample [see Appendix E and Fig. 4(c)]. Then, we employ the branched-tree growth simulation used in Fig. 3 to explore paths through the porous block. We measure the traversal time when any branch of the growing tree reaches the opposite side of the porous block. In Fig. 4, we show one simulation, where the branch network (blue) starts on the left side of the porous block and then grows, eventually traversing a path through the gray porous block to the other side. We track the traversal time for 96 simulations of each barrier density and width [Fig. 4(d)]. We find that, in qualitative agreement with the mean-field model, the traversal time increases superlinearly for increasing density. We also find a nonlinear increase in traversal time when increasing barrier width at high densities, indicating that, in real (i.e., not mean-field) systems, increasing barrier width may also increase the number of dead-end paths. Future work may explore the relative importance of material density and barrier size in other experimental systems.

V. EXPERIMENTAL TESTS OF GROWING ENTANGLEMENT

Finally, we seek to experimentally test the idea that entanglement via growth depends heavily on timescales. To do so, we use the snowflake yeast model system of undifferentiated multicellularity, which has recently been shown to evolve branch entanglement as a mechanism of generating increased multicellular toughness [23,24].

A. Altering timescales to encourage entanglement between separate clusters

One of the predictions of our entanglement models from above is that branched trees can easily grow into entangled configurations so long as they remain near each other and grow for long enough. We seek to test this prediction experimentally by growing, agitating, and imaging populations of differentially labeled (red and green) snowflake yeast. It was previously demonstrated that separate clusters do not entangle when grown in a shaking incubator at 225 rpm [23]. But, based on the above simulations, we hypothesize that separate

clusters will entangle if shaken at lower speeds, as they will spend more time in contact with each other.

To test this hypothesis, we break groups of red- and green-fluorescent snowflake yeast clusters into small pieces by compressing them between glass slides and then grow the red and green pieces in a single culture tube. After incubation, we vortex-mix each tube to ensure that any observed entanglements are mechanically stable and then image clusters to determine if distinct red and green clusters become entangled. Since we have no method for determining if same-color entanglements (i.e., entanglements between green-green or red-red clusters) are present, we count only the known entanglements (i.e., entanglements between green and red clusters) and normalize by the total number of clusters observed. We determine the experimental error via an empirical control where we expect no entanglement to occur; we culture red- and green-fluorescent strains in separate tubes overnight, then mix them in a single vial, and image them immediately. All error bars in Fig. 5 are from this control experiment.

When incubated in growth medium at low and medium shaking speeds (50 and 150 rpm, respectively), entanglement between distinct red and green clusters readily occurs [15%, $N = 273$ and 14%, $N = 299$ of examples in Fig. 5(a)], quantified by the relative proportions of combination-colored clusters compared to the total number of clusters [Fig. 5(b); see Appendix B]. At high shaking speeds (250 rpm), entanglement is rare. This stark difference occurs because, at 50 and 150 rpm, yeast clusters remain settled near the bottom of the tube, presumably interacting with the same neighboring trees for multiple rounds of cell division (see Supplemental Material Movies 1–3 [35]). At 250 rpm, clusters are dispersed throughout the fluid and, therefore, pairs of clusters do not stay near each other for sufficient times to grow entangled.

To directly test the effect of growth compared to mechanical agitation alone, we incubate some samples in a saline solution that inhibits cell division but keeps cells alive. In the experiments with growth media, snowflake yeast clusters start small but grow to large sizes. We, thus, perform controls in saline solution for both small clusters and large clusters, with size distributions matching the start and end points of the growth experiment; i.e., we perform experiments with both small (broken) clusters and large (unbroken) clusters. In all cases where we observe entanglement via growth (i.e., low and medium shaking speeds with growth medium), the proportion of entangled red-green clusters is significantly higher in culture tubes with growth than in those without growth ($p < 0.01$, z test), suggesting that random translations and rotations of the yeast branches due to agitation are not sufficient to entangle separate clusters.

B. Genetically altering branch geometries

Our above work suggests that the phenomenology of entanglement via growth and entanglement of nonliving materials are qualitatively different. On the one hand, nonliving materials entangle only if they are situated near the geometric "sweet spot" [2]. On the other hand, our simulations (Figs. 3 and 4) predict that entanglement via growth can occur even for branching geometries that are far from the sweet spot if the organisms are given enough time to grow. In other words, nonliving materials entangle only with optimal geometries,

while we predict that entanglement via growth can occur even with geometries that are far from optimal. In this section, we test these ideas experimentally.

To do so, we genetically engineer two different strains of microscopic snowflake yeast, each with a different budding geometry. The first mutant is created by knocking out the gene *ace2* in single-celled yeast; this is the "ancestral" strain used for the multicellularity long-term evolution experiment (MuLTEE) [23]. This strain of snowflake yeast tends to produce distally polar buds with fairly regular polar angles of $\langle \theta \rangle = 34 \pm 17°$ (Fig. 8). The second mutant is created by knocking out the genes *rsr1* and *ace2*. Previous works have shown that knocking out the gene *rsr1* causes buds to appear in random locations on the yeast cell surface [36]. In our engineered mutants, the mean budding angle is $\langle \theta \rangle = 57 \pm 31°$, which is a broader distribution than in the *ace2* snowflakes ($p = 0.005$, $t = 2.9$, $df = 40$, two-sample t test; see Fig. 8). Importantly, neither of these mutants entangle; mechanical stresses cause inter-cellular bonds to fracture, splitting the organism into separate pieces [25,26].

We next determine if clusters with these different budding angle geometries can entangle. We previously demonstrated that a mutation set (*clb2, cln3, gin4*), here called *mac*, can cause the *ace2* mutant to entangle [we repeat these measurements anew here, Figs. 5(c) and 5(d)] [23]. When we create this mutant strain of snowflake yeast with highly elongated cells and stronger intercellular bonds, mean group diameter increases by a factor of 14.9 [Figs. 5(c) and 5(d), $p \ll 0.001$, two-sided t test, $df = 600$, $t = -33.5$], which corresponds to a change in volume of > 1000-fold. In prior work, we have shown that the onset of entanglement leads to a similar increase in group volume [23]. Therefore, we use such an increase in group size as a proxy for entanglement. If entanglement via growth requires budding angle geometry to be near a geometric sweet spot, then a snowflake yeast mutant with *rsr1* and *mac* (i.e., *ace2 + rsr1 + clb2 + cln3 + gin4*) should not entangle, since the budding angle distribution is quite different and more spread. However, if adding the *mac* mutations to an *rsr1* mutant does result in entanglement, this would experimentally demonstrate that entanglement via growth can occur for a wide range of geometries.

We next construct the *ace2 + rsr1 + mac* mutant and measure its size. In agreement with our predictions from simulations, we find that *rsr + mac* mutants do, in fact, entangle, increasing mean group diameter by a factor of 18.3 [Figs. 5(c) and 5(d), $p \ll 0.001$, $t = 60.6$, $df = 1053$, two-sided t test]. This test, therefore, confirms that the original snowflake yeast budding geometry is not necessary for entanglement to proceed. Instead, entanglement via growth can occur for various budding geometries, including those that have been randomized and are potentially far from any sweet spot.

VI. DISCUSSION

Here, we use a combination of experiments, simulations, and theory to show that growth of branching, rigid trees more readily leads to entanglement than agitation alone. We argue, and experimentally find, that growth can produce effectively inaccessible configurations (i.e., ones that are impossible to disassemble). In simulations and experiments, we show that branching growth readily accesses these configurations, even without evolved sensing

behaviors. Finally, while geometric properties such as branch diameter clearly play a role in the frequency and strength of entanglements, we show through numerical methods that, given the right conditions for entanglement to occur, growth inexorably tunnels into configurations that are impossible to access via agitation alone. Combined, this evidence supports the idea that entanglement in growing systems is relatively easy to achieve and more dependent on timescales than geometry. Future work may explore how this effect, here studied in disordered systems, may extend to ordered systems as well.

There are two ways that nonliving systems are known to entangle. First, they can mechanically agitate separate pieces into configurations where they wrap around each other [2,3,5,37,38]. Second, entanglement can be triggered via synthesis of new bonds between previously separate chains [4,6–8]. We do not explicitly compare entanglement via growth to the latter case. But it is worth noting that entanglement triggered through new bond formation is a carefully engineered process. So far, such processes have been studied with polymers composed of modular, alternating blocks of coils and elastinlike domains [4,6], so that new bonds are selectively triggered in particular locations along the polymer. Otherwise, cross-linking of chains becomes more frequent than entanglement events, and the polymer gel loses its entanglement-derived qualities [8]. This kind of precise engineering is currently much more difficult to achieve with living systems. While extant complex multicellular organisms may be capable of the precision needed for selectively cross-linking entanglements, entanglement through growth is likely a more relevant mechanism for establishing entanglements in simple or nascent multicellular groups.

It was recently demonstrated that, even in cross-linked gels, entanglement is responsible for increased toughness [4,6,8]. Material toughness is an important property for many organisms and organism collectives, especially those that need to avoid fracture. For instance, toughness is an important characteristic of cartilage [39] and other collagen networks [40], especially as joint degeneration progresses with age or injury [41]. Animal collectives are also shown to actively entangle by bending limbs [16,37] as a mechanism for holding themselves together under external stresses like shear flows. Therefore, even in living systems where cross-linkers are known and studied, accounting for entanglement may be important.

In this paper, we show that entanglement is a common and robust phenomenon in living systems that grow as branching trees with permanent cell-cell bonds. Such bonds are a frequent evolutionary outcome in the transition to multicellularity, as exemplified by fungi, plants, red, green, and brown algae, and filamentous bacteria [42]. We demonstrate that entanglement via growth does not depend on specific geometries or morphologies but rather on the timescales of growth and interactions. Indeed, within the snowflake yeast model system, entanglement evolves within just 3000 generations of selection for larger size [23]—a geological blink of an eye. Rather than requiring substantial developmental innovation, we suggest that entanglement may be one of the first mechanisms evolved by branching multicellular organisms under selection to grow tough bodies capable of withstanding internal strains from cell division or external stresses from the environment. Despite the ease with which entanglement can evolve and its convergent evolution across many multicellular

clades, much remains to be discovered about the role of entanglement as a mechanism for generating tough, strong, multicellular materials.

Supplementary Material

Refer to Web version on PubMed Central for supplementary material.

ACKNOWLEDGMENTS

APPENDIX A: CULTURING AND SAMPLE PREPARATION

Multicellular yeast groups are sampled from an ongoing long-term evolution experiment (MuLTEE [23]). These anaerobic multicellular yeast clusters are evolved from an ancestral multicellular "snowflake" petite yeast without a functional copy of the gene *ace2*. When the *ace2* gene is not expressed, the final stage of cell division is not completed, and mother-daughter cells remain attached at the chitinous bud site. Since all cells are attached directly to their mothers, snowflake groups form a fractal-like branched-tree collective.

Yeast is generally cultured in 10 mL YEPD media [10 g yeast extract, 20 g peptone, 20 g dextrose for 1 L deionized (DI) water]. To keep yeast alive yet prevent further growth, we use a saline solution of 0.85% sodium chloride dissolved in DI water. Glass culture tubes are then cultured overnight at 30 °C in a variable-speed shaking incubator (Symphony Incubating Orbital Shaker model 3500I). We select 50, 150, and 250 rpm shaking speeds to vary the agitation strength.

1. Mechanical agitation and population size measurements

To test if mechanical agitation could disassemble grown yeast clusters, yeast clusters are first grown in overnight culture, then agitated, and then imaged to obtain a population-level size distribution. After culturing, we use wide-bore 1000 μL tips to pipette 1 mL of culture (making sure to gently shake first) into two different microcentrifuge tubes. Each tube is vortexed once at medium vortex speed (5, VWR minivortexer) for 5 s. Then, one tube is left without any more vortexing, and the other is vortexed for an additional 5 s at a stronger vortexing speed (7). 100 μL is sampled from each tube into fluorodishes, so that the clusters are not flattened by a microscope slide, and imaged under bright field using a Zeiss Axio Zoom V16 microscope.

After imaging, custom MatLab scripts segment and binarize the clusters from the background. These scripts use a combination of watershedding, morphological segmentation, and filtering to separate proximate clusters (code attached). Cluster cross-sectional area is measured and used to estimate cluster diameter using a spherical approximation.

2. Fluorescent tagging

To visualize entanglements between different groups of snowflake yeast, we isolate a single snowflake genotype from PA2, t600 (strain GOB1413-600), and engineer it to constitutively express either green- or red-fluorescent proteins. To do that, we amplify the prTEF-GFP-NATMX construct from a pFA6a-eGFP plasmid and the prTEF-dTOMATO-NATMX construct from a pFA6a-tdTomato plasmid. We then separately replace the URA3 open reading frame with GFP or dTOMATO constructs in an isogenic single-strain isolate following the LiAc transformation protocol [43]. We select transformants on nourseothricin sulfate (Gold Biotechnology Inc., U.S.) YEPD plates and confirm green- or red-fluorescent protein activity of transformed macroscopic clusters by visualizing them under a Nikon Eclipse Ti inverted microscope.

3. Genetic manipulation of geometry

To manipulate snowflake geometry, gene deletions are performed using standard polymerase chain reaction-product-based yeast transformation techniques [44]. Plasmid pYM25 bearing the hphNT1 gene for hygromycin resistance, pYM42 bearing natNT2 for nourseothricin resistance, and plasmid pYM27 bearing kanMX4 for G418 resistance are used as polymerase chain reaction templates [45] for the deletion of genes using oligonucleotides with 50 base pairs of flanking sequence from around each reading frame. Each gene is deleted individually in the Y55 homozygous diploid background previously used in the Ratcliff laboratory [46] or the multicellular GOB8 *ace2* *∷KANMX/ace2* *∷KANMX* strain created from the same background. Random budding small clusters (strain X, genotype *ace2* *∷KANMX/ace2* *∷KANMX, rsr1* *∷natNT2/rsr1* *∷natNT2*), quadruple mutants (strain AJB770, genotype ace2 *∷KANM/ace2* *∷KANMX, cln3* *∷hphNTI/cln3* *∷hphNTI, clb2* *∷kanMX4/clb2* *∷kanMX4, gin4* *∷natNT2/gin4* *∷natNT2*), and quintuple mutants (strain AJB799, genotype *ace2* *∷kanMX4/ace2* *∷kanMX4, cln3* *∷ hphNTI/cln3* *∷hphNTI, clb2* *∷kanMX4/clb2* *∷ kanMX4, gin4* *∷hphNTI/gin4* *∷hphNTI, rsr1* *∷natNT2/rsr1* *∷natNT2*) are constructed by repeated sporulation and mating of these single-deletion strains.

4. Mixed culture preparation

First, two separate tubes of green- and red-fluorescent yeast are grown overnight. Then, 150 μL is sampled from each tube. The sample is spun down in a centrifuge, and the YEPD supernatant is removed via pipetting. 300 μL DI water is added, and the spin-down-rinse cycle is repeated. 100 μL is immediately transferred to a tube containing 10 mL saline solution; these are the large controls. The remaining 200 μL is centrifuged, and most water is pipetted away. The remaining paste is transferred onto a sterilized glass microscope slide. Another slide is placed on top, and fingertip pressure and shear are added to break the snowflake yeasts into small pieces. The crushed paste is rinsed with sterile DI water into a microcentrifuge tube. 100 μL is transferred each into culture tubes containing YEPD and saline solution, forming the growing sample and the small control, respectively. All three culture tubes are then placed in the shaking incubator overnight. This process is repeated anew for each shaking speed tested.

APPENDIX B: CONFOCAL MICROSCOPY

To make a population-level measurement of entanglement likelihood, we take population-level images via confocal microscopy. First, 100 μL is sampled from each culture tube and vortexed to ensure observation of only strong entanglements. The sample is then pipetted onto microscope slides with a shallow, round depression so that clusters are not crushed by the microscope cover slips. The population is then imaged using a confocal microscope (Nikon A1R) at a few different z levels to ensure that any amount of fluorescence is captured. The z stacks are later compressed into a maximum intensity projection for each color channel.

1. Counting red, green, and tangled clusters

Transmission field images are segmented using custom MatLab scripts. Within each segmented region, color channels are binarized. We could, therefore, count the number of pixels considered red, and the number considered green, for each segmented region. If the fraction of pixels colored red exceeds a threshold value, the cluster is labeled red. Simultaneously, if the fraction of pixels colored green exceeds a threshold value, the cluster is labeled green. If neither red nor green pixel fractions exceed the threshold value, then the cluster is labeled as unknown and is discounted from further analysis. If both red and green pixel fractions exceed the threshold value, the cluster is labeled as both red and green and considered entangled. For each experiment, this threshold value is tuned to maximize image analysis efficiency. After preliminary image analysis, clusters that are labeled as entangled are visually checked for accuracy.

To gauge the population-level fraction of all clusters that are entangled, we count the number of clusters labeled each type. Out of all clusters imaged from a population N, there are some labeled entirely red N_r, some labeled entirely green N_g, and some labeled both red and green N_e, such that $N = N_r + N_g + N_e$. In the main text, we report the proportion of clusters that are entangled as N_e/N. However, based on initial concentrations and growth rates, it is possible that, for different experiments, the initial number of red and green clusters in one tube is different. To account for this difference, the fraction of all entangled clusters, N_e/N, is normalized by the smaller value of either N_r/N or N_g/N for each shaking speed, as in $n_e = N_e/N_r$. Notably, no p values change from nonsignificant to significant, or vice versa, by using this correction. We report this calculation in Fig. 6. Note that, since our measurement method can detect if two separate clusters become entangled only if they are different clusters, we do not count any entirely red or entirely green clusters as being entangled. Therefore, we likely undercount the total amount of entanglement occurring in the tube.

Because the counting analysis method fundamentally relies on cluster proximity, it is possible that two separate, nonentangled clusters, one red and one green, happen to locate next to one another for imaging, such that the analysis algorithm counts the pair as entangled even though they are not. To measure this experimental imprecision, we run a control experiment where we do not expect entanglement to occur. Separated red and green clusters are pipetted into the same microcentrifuge tube and then immediately imaged without

allowing time for growth. The measured value for n_e for this experiment is 0.033 and is taken as the experimental error for the remaining experiments.

APPENDIX C: SCANNING ELECTRON MICROSCOPY

Since yeast cells have thick cell walls that limit the effectiveness of optical microscopy, we use scanning electron microscopy to obtain three-dimensional structural information. We use data from the same experiments reported in Refs. [23,32]. In those experiments, we use a Zeiss Sigma VP 3View scanning electron microscope (SEM) equipped with a Gatan 3View SBF microtome installed inside a Gemini SEM column to obtain high-resolution images of the internal structure of snowflake yeast groups and locate the positions of all cells. All SEM images are obtained in collaboration with the University of Illinois's Materials Research Laboratory at the Grainger College of Engineering. Snowflake yeast clusters are grown overnight in YPD media, then fixed, stained with osmium tetroxide, and embedded in resin in an Eppendorf tube. A cube of resin 200 μm × 200 μm × 200 μm (with an isotropic distribution of yeast clusters) is cut out of the resin block for imaging. The top surface of the cube is scanned by the SEM to acquire an image with resolution 50 nm per pixel (4000 × 4000 pixels). Then, a microtome shaves a 50-nm-thick layer from the top of the specimen, and the new top surface is scanned. This process is repeated until 4000 images are obtained so that the data cube has equal resolution in x, y, and z dimensions.

The resulting voxel representation of the interior of one cluster is then binarized and segmented using custom PYTHON scripts. Connected cells are identified using the nearest-neighbor algorithm. From a particular subvolume of the data cube, we identify 38 connected components, which we call branches, that are not connected to one another except through mechanical tangling events. Surface data of each branch are obtained by using the surface mesh tool in *Mathematica* 12, as previously described in Ref. [23]. New to this study, the surfaces are imported into Blender and remeshed using the Blender remesh tool to lower the total number of data points on the surface. This allows for faster computation speeds. Then, alpha shapes of these branches are created. Alpha shapes are a generalization of the convex-hull method that allows for nonconvex shapes. The alpha value can be tuned to allow for more or less concavity of the shape. But, furthermore, there are fast algorithms for computing intersections of alpha shapes, which are desirable here.

APPENDIX D: 3D STRUCTURAL CONSTRUCTION AND MANIPULATIONS

We choose several individual branches from our list to perform computational manipulations as described in the main text. These manipulations involve either translations or rotations of all points representing the branch, which are carried out via matrix multiplication schemes. All of these manipulation algorithms are written as custom functions in MatLab.

Random rotations and translations are constructed as follows. Random translation steps are sampled from a uniform distribution on the domain [−0.5, 0.5], for each coordinate x, y, and z. Then, the resulting vector is normalized to have length a, where a is the step size input. Random rotations are created by first choosing a random axis and then rotating by a chosen angle magnitude around this axis. The rotation axis is randomly chosen by selecting

a random number from a uniform distribution on the domain [−0.5, 0.5] for each coordinate *x*, *y*, and *z* and then normalized to have unit magnitude.

During our mechanical agitation procedures, overlapping volumes are calculated using MatLab's built-in alpha shape capabilities, which allows for fast and accurate computations.

1. Choosing a threshold for the point of first contact

For drag experiments, we choose a threshold overlapping volume of 1 cubic micron that marks the "point of first contact." We choose this value because it is close to a value for which the force exerted on each cell is $1/10$ the magnitude of force previously measured to fracture bonds between snowflake yeast cells [26]. Following a Hertzian model of an elastic material, the force exerted by overlapping two elastic spheres of equal radius *r* by a distance *d* is $F = 4/3Y\sqrt{(r/2)}d^{3/2}$, where *Y* is Young's modulus. The volume of overlap between the two spheres is $V = \pi=12(2r - d)d^2$. Inputting a force of 0.05 μN, a Young's modulus of 1 MPa, and an effective radius of 5 μm, we solve for the appropriate deflection and find an overlapping volume of 0.05 cubic microns. Multiplied by 20 cells, about the number of cells in the entangled branches, returns a net overlapping volume value of 1 cubic micron.

2. Measuring bud scar angle distributions

Bud scar angle distributions are measured for two strains: ancestral, *ace2* knockout yeast cells, and *ace2 rsr1* genetic mutants. Clusters are cultured overnight in separate YEPD tubes at 30 °C and 250 rpm shaking speed. The next day, bud scars (which are rich in chitin) are stained with calcofluor white. To stain the cells, we take a 500 μL sample of each tube, then centrifuge them and remove the supernatant, and resuspend the sample in sterile DI water. We repeat this process once more but this time do not resuspend the pellet. Then, 15 μL of 1 mg/mL calcofluor stock is diluted in 500 μL 1×phosphate buffer solution. 250 μL of the prepared calcofluor solution is added on top of the two pellets. After vortexing, we incubate the tubes in darkness at room temperature for 25 min. The tubes are centrifuged, the pellets removed, and the cells are resuspended in sterile DI water. Then, 30 μL is sampled from each tube onto separate glass slides and taken for imaging on a Nikon A1R confocal microscope with a 60× oil objective. We use a 450 nm wavelength laser to excite the calcofluor stain and take *z* stacks of cells to obtain three-dimensional bud scar information. We examine nine ancestral, *ace2* cells and 12 *ace2 rsr1* mutant cells, each with two bud scars in addition to their one birth scar. Custom Fiji and MatLab scripts segment the cells, fit an ellipsoid of revolution to each, segment the bud scars (which fluoresce very brightly), and measure their polar orientation with respect to a birth scar that is always located at the south pole of the cell. The polar angle measured here is 0° at the north pole, 90° at the equator, and 180° at the south pole. The distribution of polar angles is reported in Fig. 8.

3. Measuring group size

To measure group size of each of the four strains of yeast clusters, groups are grown overnight in YEPD at 30 °C and 250 rpm shaking speed. Then, 500 μL are sampled from

each tube into a fluorodish so that clusters are not broken into pieces by a glass coverslip. We then image the clusters on a Zeiss Axio Zoom V16 microscope. Custom scripts segment the clusters from these images and measure their cross-sectional area. This area is used to calculate an effective diameter via $d = 2 * \sqrt{A/\pi}$.

4. Measuring single cell size

To measure the single cell size of ancestral *ace*2 yeast cells and randomly budding *rsr*1 cells, yeast clusters are imaged on a Nikon widefield inverted microscope with a 40× objective. Ten individual cells are segmented from these images, and their maximum diameter is measured using the Fiji length measurement tool. The ancestral snowflake yeast cells have a mean measured diameter of 7.0(8) μm, and the randomly budding mutant has measured mean diameter 6.6(3) μm. A two-sample *t* test returns $t = 1.54$, $df = 18$, and $p = 0.14$.

APPENDIX E: BRANCHED-TREE SIMULATIONS

1. Growing trees

We create custom simulations for growing, branching, dendrimerlike objects in three dimensions in MatLab. We call these objects trees. Each tree is created by starting with six seed points, which represent the hyphal tip. Each hyphal tip possesses three properties: a location, an orientation, and the number of steps that have occurred since it last split. We continually track the locations and orientations of each hyphal tip; additionally, we add these locations to a growing list of tip locations for all previous time points. Each time point, all hyphal tips walk forward one unit in the direction they are oriented; their locations are then updated. A disk of a selected radius is constructed around the hyphal tip such that the plane of the disk is orthogonal to the tip's orientation. An integer number of evenly spread points within this disk are then added to the list of all locations previously occupied by the tree.

To start, all seed directions are the six cardinal directions ($-x$ and $+x$, $-y$ and $+y$, and $-z$ and $+z$). The hyphal tips then extend until they reach a threshold number of steps from their starting location. At this point, each hyphal tip splits into two tips, each occupying the same location but with different orientations. The angle between the two orientation vectors is varied between [30, 180]° for our simulations. The azimuthal orientation is randomly selected from a uniform distribution on the domain $\phi = [0, 2\pi)$. After splitting, the algorithm continues to track a (now larger) list of the hyphal tips. This process continues for a set number of iterations.

2. Deflection of branches

When branches of the same tree encounter one another, they do not interact. When branches of one tree encounter a different tree, they deflect. Collisions are detected by computing the overlapping volume of the alpha shapes of the two trees. If there is any overlap, it is identified. Then, the hyphal tip that penetrates the alpha shape of the second tree retreats a small amount (0.5 units backward). It then changes its orientation by randomly selecting an orientation orthogonal to its last orientation.

We measure the density of example grown trees by counting the number of voxels contained within the branches a distance between r and $r + \delta r$ from the center of mass and dividing that value by the total number of voxels contained within a spherical shell of the same radius and depth. We report the density maps in Fig. 9. Notably, the density of all clusters decays from the interior after this number of branching events.

We also test simulations where branches do not deflect but instead are terminated (deleted from the hyphal tip list) and others where branches deflected by 45° instead of 90°. In both cases, trees that are grown near each other do not recover their original positions (Fig. 10).

3. Mechanical agitation of branching trees

To mechanically agitate the trees, we could apply global rotations and translations to all points in the tree list. We then iteratively agitate via a combination of a translation of two units in a random direction and a rotation of 2° around a random axis, check for alpha shape collisions between two trees, and accept or reject the agitation. Each agitation is accepted if either (i) it results in a smaller overlapping volume than in the previous agitation step or (ii) with a Boltzmann probability $p = e^{-\Delta V/T}$, where $\Delta V = V_i - V_{i-1}$ is the difference between current and previous overlapping volumes, with annealing temperature $T = 10$ units, which is generally restrictive (moves that increase overlapping volume are rejected 64% of the time). If the move is accepted, it is stored as the current state of the tree. If it is rejected, we restore the last known state of the tree and continue the agitation process.

Agitation experiments generally have two stages. First, the trees are pushed together until they collide. Then, trees are agitated as described in the above paragraph for a set number of iterations. Then, the trees are again pushed together, and again agitated, etc. The number of thermal agitation steps is 25 used in the main text; we also test using 100 thermal steps, which we find does not change the results (Fig. 11). Furthermore, we find diminishing returns for continued cycles of pushing and jiggling; we decide to terminate the simulations after 25 cycles based on these results (Fig. 11).

4. Controlling for morphological differences between grown and pushed trees

We next control for morphological differences between trees that are grown separately and trees that are grown close to each other. We collect pairs of trees that are grown at a close separation distance and separate them by a far distance ($2L_0$). We then use the same pushing agitation procedure outlined above to push them together. Rather than achieving their original, close configuration (approximately 50 units) once again, we find that trees achieve an average minimum distance of 87.5 ± 8.1 ($0.91L_0$) units. This value is similar to the average minimum distance achieved by trees undergoing solely agitation ($p = 0.29$, $z = -1.06$), indicating that the close configuration is truly inaccessible to agitated trees. In none of the 134 instances do trees reach the same or closer distance through agitation than they do through growth.

5. Measuring entanglement for a range of different growth geometries

To explore the probability of entanglement for growing hyphal trees of different geometric properties, we grow trees nearby and then "drag" them apart to measure collisions. First, we grow one tree in isolation with a selected value of Λ and θ that defines its geometric properties as described above, for a length of time $B = 4$ which means that growth is truncated at four branching events. The farthest reach of this tree is measured as $r_{\max} = \mathbf{max}(|r - \bar{r}|)$, where r is a list of the Cartesian coordinates of the tree volume, $\bar{r}$ is the center of mass position of the tree, and $|\cdots|$ denotes the vector magnitude. A random point on the surface of a sphere with radius $r_{\max}$ is selected to be the initial seed point of a second tree, which is then grown with the same values of Λ and θ and for a length of time B which is varied from 3 to 6.

100 cases of each growth time B and geometric property pair (Λ, θ) are simulated. After growth, the simulations are checked for entanglement via a drag experiment. First, the centers of mass ($\bar{r}_1$ and $\bar{r}_2$) are found for both trees. The vector $r_{\mathrm{pull}} = \bar{r}_2 - \bar{r}_1$ pointing from tree 1 to tree 2 is defined as the dragging axis. Then, the second tree is pulled along that axis away from tree 1 in steps of length 2 simulation units, until they are completely separated. At each step, the overlap of the two alpha shapes is measured. Entanglement is defined to occur when there is a peak in the overlap volume greater than a threshold value of $T = \pi$ $* d^3$ or the volume of a cylinder with radius $d/2$ and height d, where d is the diameter of the branches. This drag experiment is repeated for all 100 simulations of each geometric and growth time value, and the proportion of entangling simulations is measured.

6. Tunneling hyphae

We also use a modified version of the branched-tree simulations to test predictions of our tunneling model. In these simulations, hyphae began as one hyphal tip growing in the positive x direction. Then, hyphal tips would extend and periodically split, as described above. For the tunneling simulations, the hyphal tips interact with a porous medium rather than with another tree. Additionally, the number of simultaneous hyphal tips is capped at 500 for computational speed. When the number of tips exceeds 500, some tips are pruned (deleted from the list) until the number of tips is below 500.

The porous medium used for these simulations is a subsampled block of data taken from the SEM experiments of the snowflake yeast. This subsampled, voxelized block of data contains yeast cells at a packing fraction of $\phi = 0.38$. The block is truncated at various depths to obtain different porous medium widths. To obtain different volume fractions, the voxelized dataset is eroded or dilated (using MatLab algorithms for binary image erosion and dilation) with a cubic kernel. For different sized kernels, we erode or dilate to different volume fractions, allowing for densities ranging from 0.004 to 0.711, calculated by dividing the number of voxels considered "on" by the total number of voxels within the sample block. These densities are normalized by the bond percolation critical value for cubic lattices in three dimensions, $p_c = 0.7530$ [33,34].

References

[1]. Raymer DM and Smith DE, Spontaneous knotting of an agitated string, Proc. Natl. Acad. Sci. U.S.A 104, 16432 (2007). [PubMed: 17911269]

[2]. Gravish N, Franklin SV, Hu DL, and Goldman DI, Entangled granular media, Phys. Rev. Lett 108, 208001 (2012). [PubMed: 23003190]

[3]. Brown E, Nasto A, Athanassiadis AG, and Jaeger HM, Strain stiffening in random packings of entangled granular chains, Phys. Rev. Lett 108, 108302 (2012). [PubMed: 22463461]

[4]. Tang S, Glassman MJ, Li S, Socrate S, and Olsen BD, Oxidatively responsive chain extension to entangle engineered protein hydrogels, Macromolecules 47, 791 (2014). [PubMed: 24910474]

[5]. Meng L, Wang C, and Yao X, Non-convex shape effects on the dense random packing properties of assembled rods, Physica (Amsterdam) A490, 212 (2018).

[6]. Edwards CER, Mai DJ, Tang S, and Olsen BD, Molecular anisotropy and rearrangement as mechanisms of toughness and extensibility in entangled physical gels, Phys. Rev. Mater 4, 015602 (2020).

[7]. Norioka C, Inamoto Y, Hajime C, Kawamura A, and Miyata T, A universal method to easily design tough and stretchable hydrogels, NPG Asia Mater. 13, 34 (2021).

[8]. Kim J, Zhang G, Shi M, and Suo Z, Fracture, fatigue, and friction of polymers in which entanglements greatly outnumber cross-links, Science 374, 212 (2021). [PubMed: 34618571]

[9]. Marenduzzo D, Micheletti C, and Orlandini E, Bio-polymer organization upon confinement, J. Phys. Condens. Matter 22, 283102 (2010). [PubMed: 21399272]

[10]. Meluzzi D, Smith DE, and Arya G, Biophysics of knotting, Annu. Rev. Biophys 39, 349 (2010). [PubMed: 20192771]

[11]. Wischnewski A, Monkenbusch M, Willner L, Richter D, Likhtman AE, McLeish TCB, and Farago B, Molecular observation of contour-length fluctuations limiting topological confinement in polymer melts, Phys. Rev. Lett 88, 058301 (2002). [PubMed: 11863784]

[12]. Everaers R, Sukumaran SK, Grest GS, Svaneborg C, Sivasubramanian A, and Kremer K, Rheology and microscopic topology of entangled polymeric liquids, Science 303, 823 (2004). [PubMed: 14764875]

[13]. Hou J-X, Svaneborg C, Everaers R, and Grest GS, Stress relaxation in entangled polymer melts, Phys. Rev. Lett 105, 068301 (2010). [PubMed: 20868018]

[14]. Padding JT and Briels WJ, Systematic coarse-graining of the dynamics of entangled polymer melts: The road from chemistry to rheology, J. Phys. Condens. Matter 23, 233101 (2011). [PubMed: 21613700]

[15]. Panagiotou E, Millett KC, and Atzberger PJ, Topological methods for polymeric materials: Characterizing the relationship between polymer entanglement and viscoelasticity, Polymers 11, 437 (2019). [PubMed: 30960421]

[16]. Hu D, Phonekeo S, Altshuler E, and Brochard-Wyart F, Entangled active matter: From cells to ants, Eur. Phys. J. Special Topics 225, 629 (2016).

[17]. Becker K, Teeple C, Charles N, Jung Y, Baum D, Weaver JC, Mahadevan L, and Wood R, Active entanglement enables stochastic, topological grasping, Proc. Natl. Acad. Sci. U.S.A 119, e2209819119 (2022). [PubMed: 36215466]

[18]. Patil VP, Tuazon H, Kaufman E, Chakrabortty T, Qin D, Dunkel J, and Bhamla MS, Ultrafast reversible self-assembly of living tangled matter, Science 380, 392 (2023). [PubMed: 37104611]

[19]. Hallatschek O, Datta SS, Drescher K, Dunkel J, Elgeti J, Waclaw B, and Wingreen NS, Proliferating active matter, Nat. Rev. Phys 5, 407 (2023).

[20]. https://cstremblog.blogspot.com/.

[21]. https://commons.wikimedia.org/wiki/File:Prototaxm10.JPG.

[22]. http://www.davidmoore.org.uk/Sec01_03.htm.

[23]. Bozdag GO, Zamani-Dahaj SA, Day TC, Kahn PC, Tong K, Balwani AH, Dyer EL, Yunker PJ, and Ratcliff WC, De novo evolution of macroscopic multicellularity, Nature (London) 617, 747 (2023). [PubMed: 37165189]

[24]. Ratcliff WC, Denison RF, Borrello M, and Travisano M, Experimental evolution of multicellularity, Proc. Natl. Acad. Sci. U.S.A 109, 1595 (2012). [PubMed: 22307617]

[25]. Ratcliff WC, Fankhauser JD, Rogers DW, Greig D, and Travisano M, Origins of multicellular evolvability in snowflake yeast, Nat. Commun 6, 1 (2015).

[26]. Jacobeen S, Pentz JT, Graba EC, Brandys CG, Ratcliff WC, and Yunker PJ, Cellular packing, mechanical stress and the evolution of multicellularity, Nat. Phys 14, 286 (2018). [PubMed: 31723354]

[27]. Røgen P and Fain B, Automatic classification of protein structure by using Gauss integrals, Proc. Natl. Acad. Sci. U.S.A 100, 119 (2003). [PubMed: 12506205]

[28]. Panagiotou E and Kauffman LH, Knot polynomials of open and closed curves, Proc. R. Soc. A 476, 20200124 (2020). [PubMed: 32922152]

[29]. Tzoumanekas C and Theodorou DN, Topological analysis of linear polymer melts: A statistical approach, Macromolecules 39, 4592 (2006).

[30]. Kröger M, Dietz JD, Hoy RS, and Luap C, The z1+ package: Shortest multiple disconnected path for the analysis of entanglements in macromolecular systems, Comput. Phys. Commun 283, 108567 (2023).

[31]. Donev A, Cisse I, Sachs D, Variano EA, Stillinger FH, Connelly R, Torquato S, and Chaikin PM, Improving the density of jammed disordered packings using ellipsoids, Science 303, 990 (2004). [PubMed: 14963324]

[32]. Day TC, Höhn SS, Zamani-Dahaj SA, Yanni D, Burnetti A, Pentz J, Honerkamp-Smith AR, Wioland H, Sleath HR, Ratcliff WC, Goldstein RE, and Yunker PJ, Cellular organization in lab-evolved and extant multicellular species obeys a maximum entropy law, eLife 11, 1 (2022).

[33]. Sykes MF and Essam JW, Critical percolation probabilities by series methods, Phys. Rev 133, A310 (1964).

[34]. Gaunt DS and Sykes MF, Series study of random percolation in three dimensions, J. Phys. A 16, 783 (1983).

[35]. See Supplemental Material at http://link.aps.org/supplemental/10.1103/PhysRevX.14.011008 for videos of snowflake yeast in culture tubes under different shaking speed conditions.

[36]. Casamayor A and Snyder M, Bud-site selection and cell polarity in budding yeast, Curr. Opin. Microbiol 5, 179 (2002). [PubMed: 11934615]

[37]. Ozkan-Aydin Y, Goldman DI, and Bhamla MS, Collective dynamics in entangled worm and robot blobs, Proc. Natl. Acad. Sci. U.S.A 118, e2010542118 (2021). [PubMed: 33547237]

[38]. Tuazon H, Kaufman E, Goldman DI, and Bhamla MS, Oxygenation-controlled collective dynamics in aquatic worm blobs, Integr. Comp. Biol 62, 890 (2022). [PubMed: 35689658]

[39]. Jackson TW, Michel J, Lwin P, Fortier LA, Das M, Bonassar LJ, and Cohen I, Structural origins of cartilage shear mechanics, Sci. Adv 8, abk2805 (2022).

[40]. Burla F, Dussi S, Martinez-Torres C, Tauber J, van der Gucht J, and Koenderink GH, Connectivity and plasticity determine collagen network fracture, Proc. Natl. Acad. Sci. U.S.A 117, 8326 (2020). [PubMed: 32238564]

[41]. Decker RS, Articular cartilage and joint development from embryogenesis to adulthood, in Seminars in Cell &Developmental Biology (Elsevier, New York, 2017), Vol. 62, pp. 50–56. [PubMed: 27771363]

[42]. Day TC, Márquez-Zacarías P, Bravo P, Pokhrel AR, MacGillivray KA, Ratcliff WC, and Yunker PJ, Varied solutions to multicellularity: The biophysical and evolutionary consequences of diverse intercellular bonds, Biophys. Rev. Lett 3, 021305 (2022).

[43]. Gietz R and Schiestl R, High-efficiency yeast transformation using the LiAC/SS carrier DNA/PEG method, Nat. Protoc 2, 31 (2007). [PubMed: 17401334]

[44]. Gietz RD and Schiestl RH, Quick and easy yeast transformation using the LiAC/SS carrier DNA/PEG method, Nat. Protoc 2, 35 (2007). [PubMed: 17401335]

[45]. Janke C, Magiera MM, Rathfelder N, Taxis C, Reber S, Maekawa H, Moreno-Borchart A, Doenges G, Schwob E, Schiebel E et al. , A versatile toolbox for PCR-based tagging of yeast genes: New fluorescent proteins, more markers and promoter substitution cassettes, Yeast 21, 947 (2004). [PubMed: 15334558]
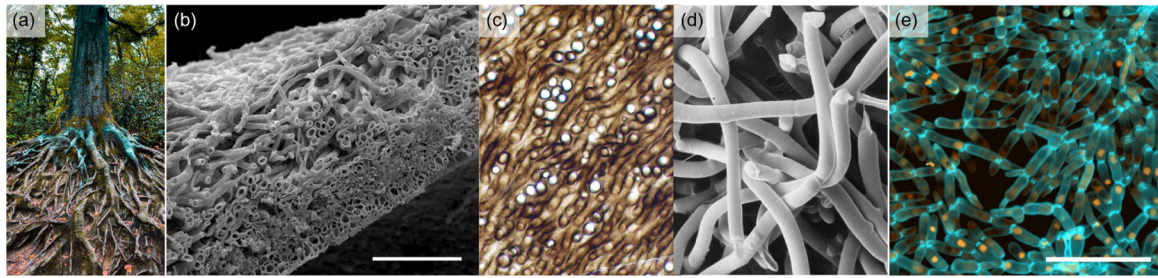
[46]. Ratcliff W, Fankhauser J, Rogers D, Greig D, and Travisano M, Origins of multicellular evolvability in snowflake yeast., Nat. Commun 6, 6102 (2015). [PubMed: 25600558]

FIG. 1.

Several examples of entangled, growing materials. (a) Tree roots winding and twisting around each other. Photo used with permission from Omar Ram via Unsplash. (b) *Peltigera membranacea*, a type of lichen, in cross section. The scale bar is 100 μm. Image source, Ref. [20]. Image used with permission from Chistopher Tomellion. (c) The fossilized (probable) fungus *Prototaxites*, which formed structures 8 m tall 400 million years ago. Strands are about 50 μm in diameter. Image source, Ref. [21]. This image is in the public domain. (d) Scanning electron micrograph of hyphae of *Pleurotus*. The hyphae have a diameter of about 3 μm. Image source, Ref. [22]. Image used with permission from Dr. Carmen Sanchez. (e) Confocal microscope image of snowflake yeast, scale bar 50 μm.
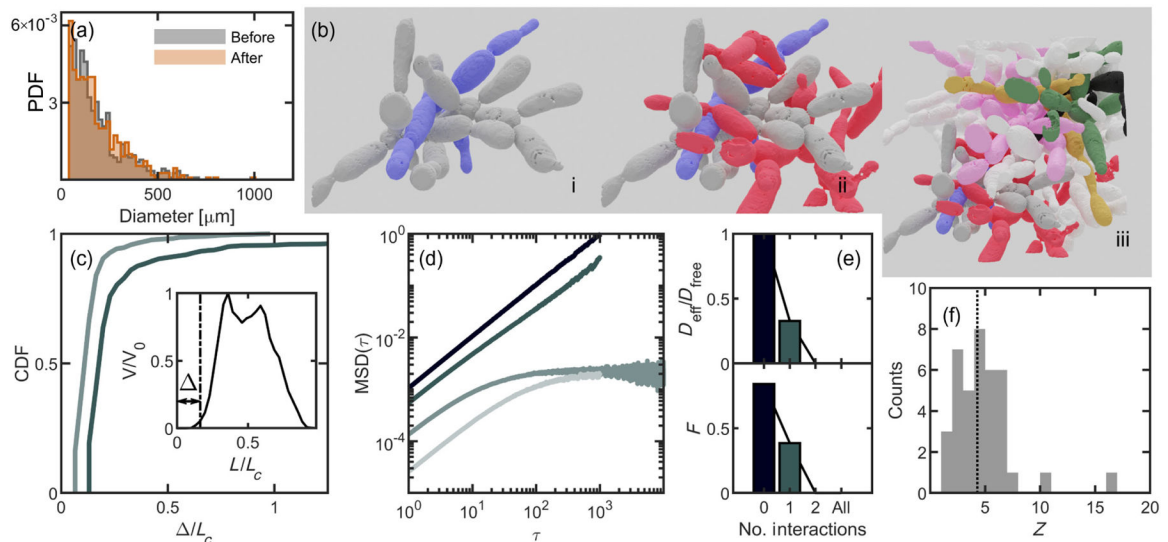
FIG. 2.

Growing branches access configurations inaccessible or difficult to access through agitation alone. (a) Histogram of yeast group sizes before and after strong agitation via vortexing. (b) Several examples of entangled branches. (i) Two pieces penetrate each other's empty space, (ii) a third piece also entangles with the previous two, and (iii) a view of all pieces identified in the sample data cube. (c) Cumulative distribution function (CDF) for the distance dragged until the point of first contact, in units of distance scaled by average cell length. Dark line, two piece interaction from (a)(i); lighter line, the three-piece interaction from (a)(ii). Inset: an example of one drag run, showing net overlap scaled by the maximum overlap and distance pulled scaled by cell length. The distance to defined first contact, , is illustrated. (d) Mean-squared displacement vs lag time for four different agitation interaction scenarios. The target piece is always the gray piece from (b). From dark to light, the lines represent free diffusion, one interaction (b)(i), two interactions (b)(ii), and all interactions (b)(iii). (e) Top, the effective diffusion constant for all lines from (d), scaled by the free diffusion constant. Bottom, the fraction of independent simulations that translate at least one cell length. (f) The coordination number for all 38 pieces from (b)(iii).
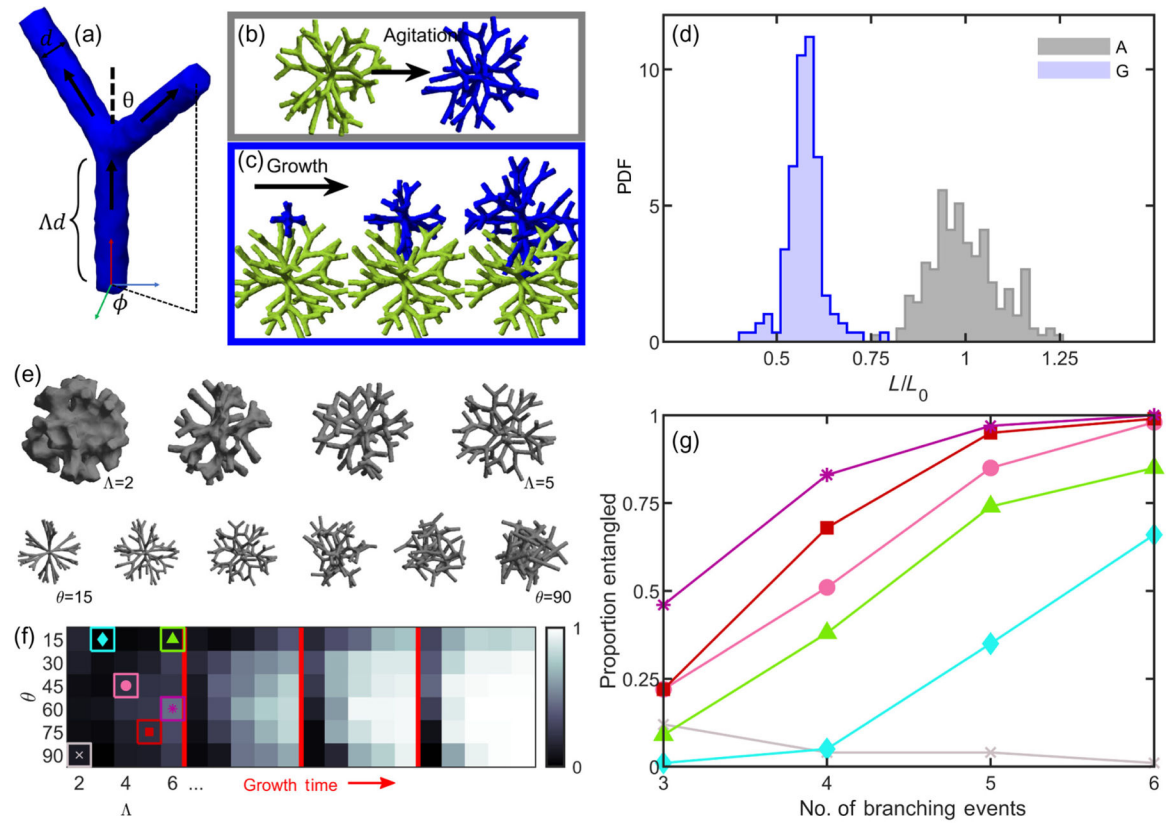
FIG. 3.

Simulations of growing branches easily entangle. (a) Illustration of a growing hyphal branch with one tip splitting into two tips, along with relevant geometric parameters. (b) Two separately generated trees are pushed together and mechanically agitated. (c) One tree is first generated, and then a second is grown nearby (three stages of growth are shown—early, middle, and late times). (d) Histograms of distances between pairs of trees centers of mass. A stands for trees grown separately and agitated; G stands for trees grown nearby. Lengths are scaled by the mean distance achieved from agitation alone. (e) Examples of individual grown trees with varying geometric parameters. Top row: varying Λ from 2 to 5; bottom row: varying θ from $15°$ to $90°$. (f) Phase maps measuring the proportion of pairs of trees that are measured as entangled. Branching geometry is varied for four different growth times. From left to right: three branching events (short times), four branching events (intermediate), five, and six. (g) Tracking trajectories of entanglement probability for the specific branching geometries highlighted in (f).
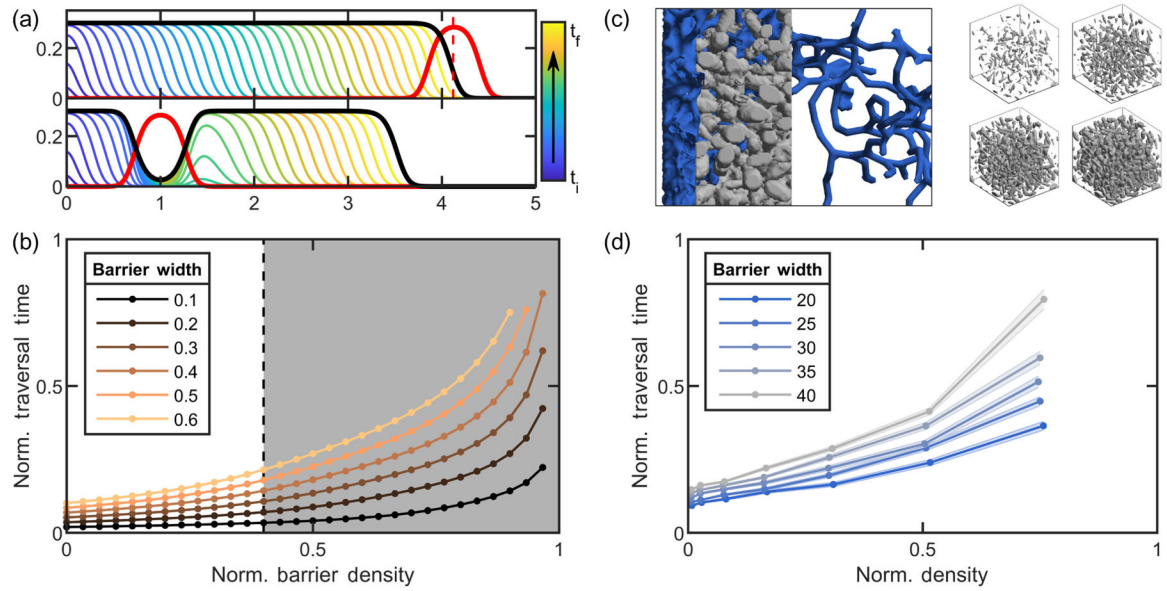
FIG. 4.

Growth ensures tunneling to states unreachable from agitation alone. (a) Two numerical solutions to Eq. (1), plotting $\rho(r)$ vs r. Top: Eq. (1) is solved in free space; then a barrier (red) is translated toward the grown density field (black) until the two-density sum exceeds ϕ_{max} at any location. The dashed line is the closest the barrier reaches. Bottom: Eq. (1) is solved when the barrier (red) is present, illustrating tunneling through the barrier. The color bar and arrow indicate the direction of proceeding time. (b) Traversal time of a square barrier vs the barrier density, from solutions to Eq. (1) for different barrier widths, normalized by maximum numerical integration time. The white region is where the square barrier density is low enough so that the barrier could be pushed completely through the grown density field, illustrating states that are accessible to agitation. The gray region is where the barrier and field cannot be pushed through each other, indicating thermally inaccessible configurations. (c) Left: example simulation of traversal of rigid, branched hyphae (blue) through a porous medium (gray). Right: examples illustrating changing density of the porous medium from 0.02 to 0.23. (d) Normalized traversal times of simulations for varying porous medium densities and widths. The x axis is scaled by the bond percolation threshold for 3D cubic lattices [33,34]. Different color lines represent means across 96 different simulations for different barrier widths. For clarity, the standard deviation in traversal times for only one barrier width is displayed.
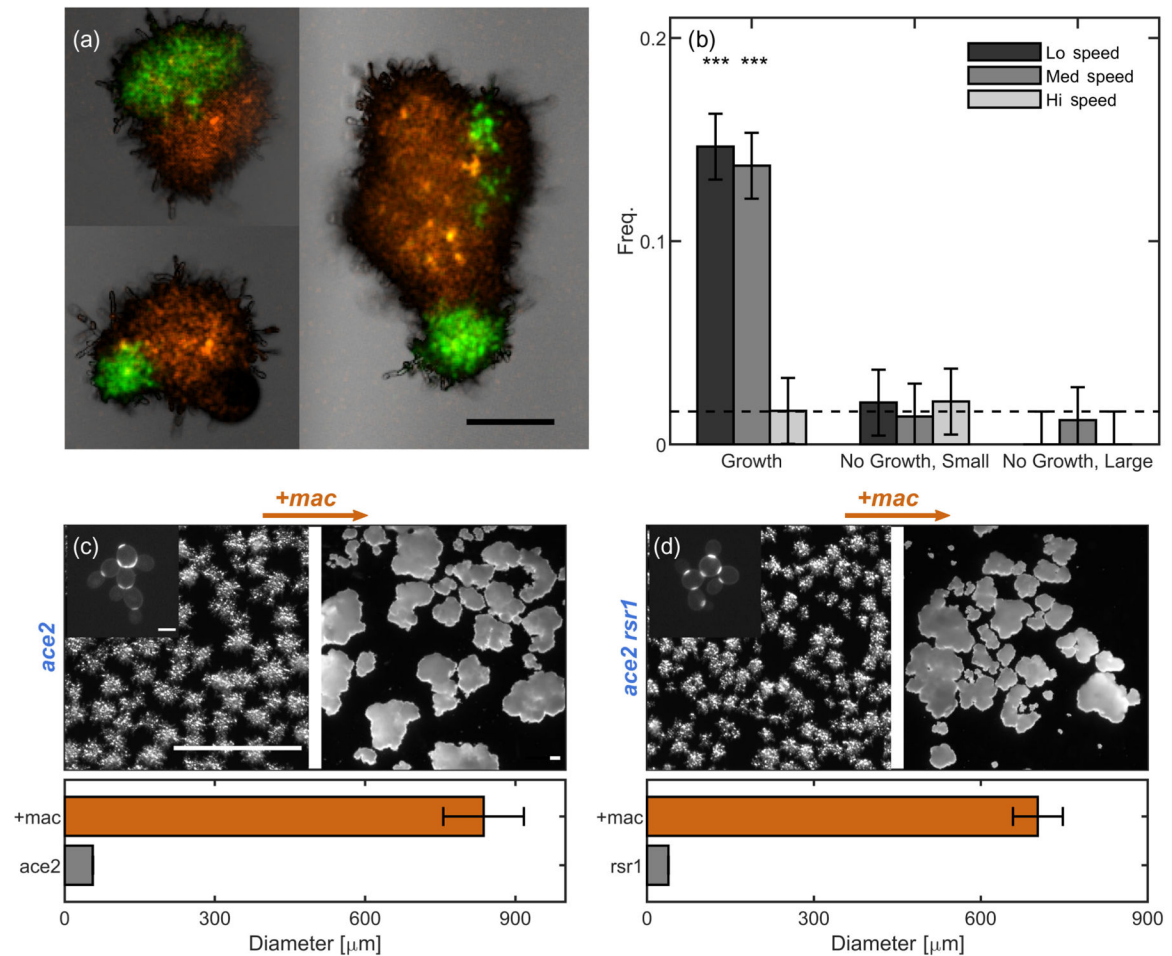
FIG. 5.

Growing branches entangle readily. (a) Three examples of combination-colored, entangled yeast clusters. The scale bar is 100 μm. (b) Proportion of clusters observed to be entangled for various treatment types, normalized by the total number of clusters. Horizontal dashed line is a measurement of algorithm error via a control where no entanglement is expected (i.e., immediately pipetting a mix of green and red clusters onto a slide without any agitation or growth). Error bars are also drawn from this empirical measurement of algorithm precision. Three stars indicate $p < 0.001$ significance level; two indicate $p < 0.01$. (c) Top left: *ace*2 snowflake yeast that does not entangle. Inset: higher-magnification image of *ace*2 stained with calcofluor white that brightly highlights bud scars to show the characteristic snowflake yeast pattern. The inset scale bar is 5 μm. Top right: We apply genetic mutation set 1 (*mac* = *clb*2 + *cln*3 + *gin*4), inducing changes that lead to entanglement. The scale bars in the top left and top right are both 300 μm. Bottom: mean diameter (and standard error) of these two strains. (d) The same information as (c) but for the mutant line *ace*2*rsr*1. The images have the same scale as their counterparts in (c).
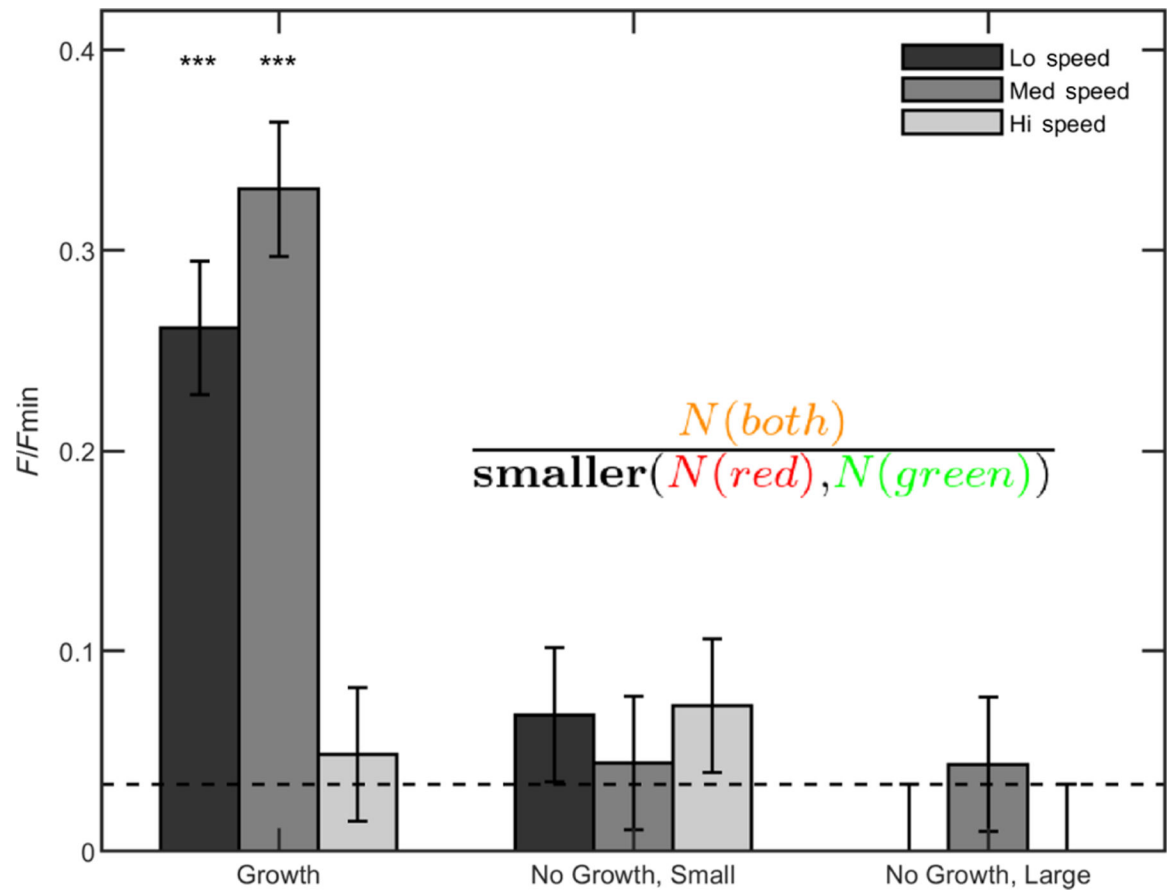
FIG. 6.
Counts of red-and-green entangled clusters are normalized by the smaller proportion of either total red or total green clusters in the field of view.
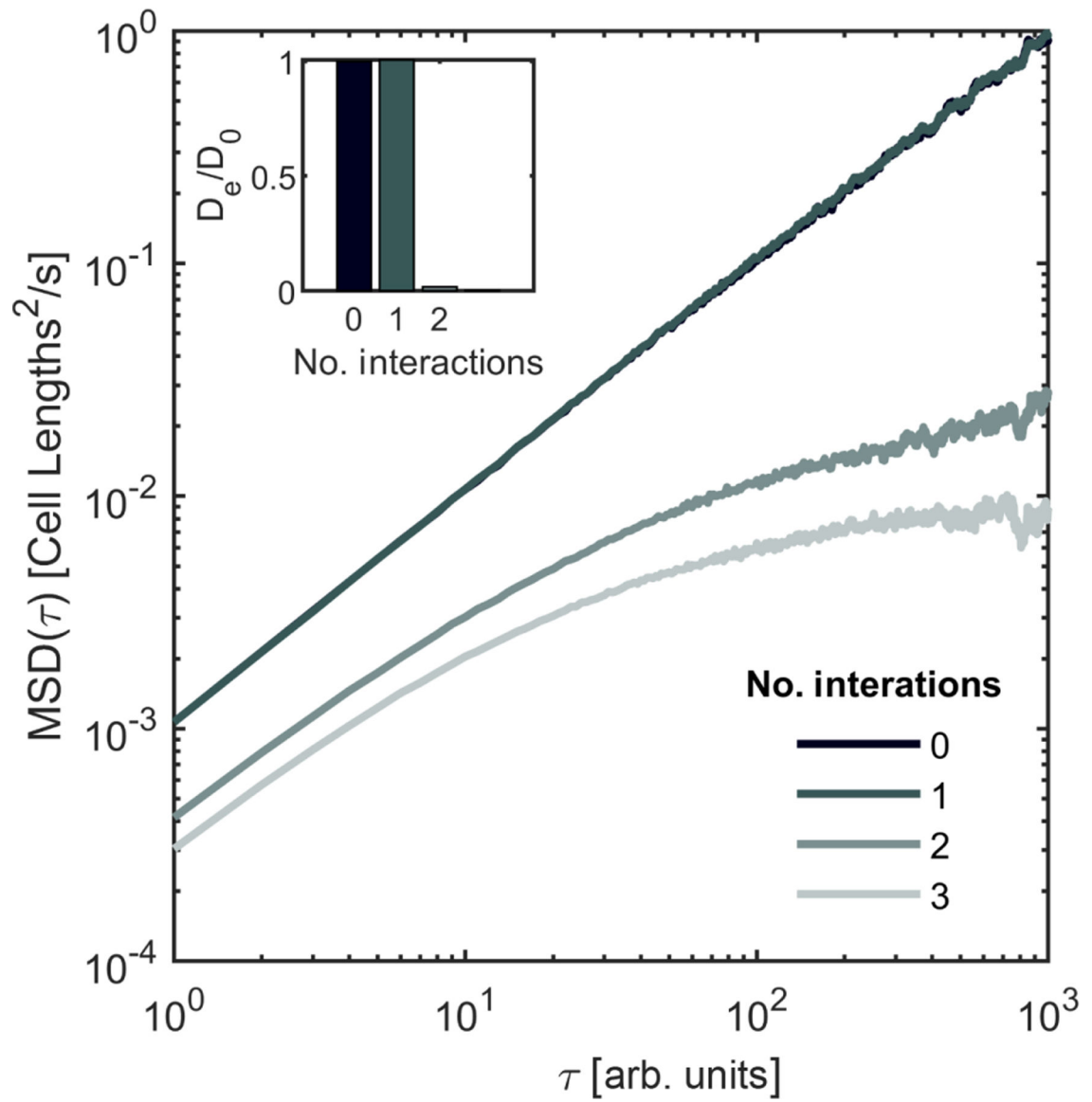
FIG. 7.

Mean squared displacement plots for four circumstances where one branch [yellow, main Fig. 2(a)(iii)] is agitated with respect to others, with zero interactions, one interacting branch, two interacting branches, and three interacting branches.
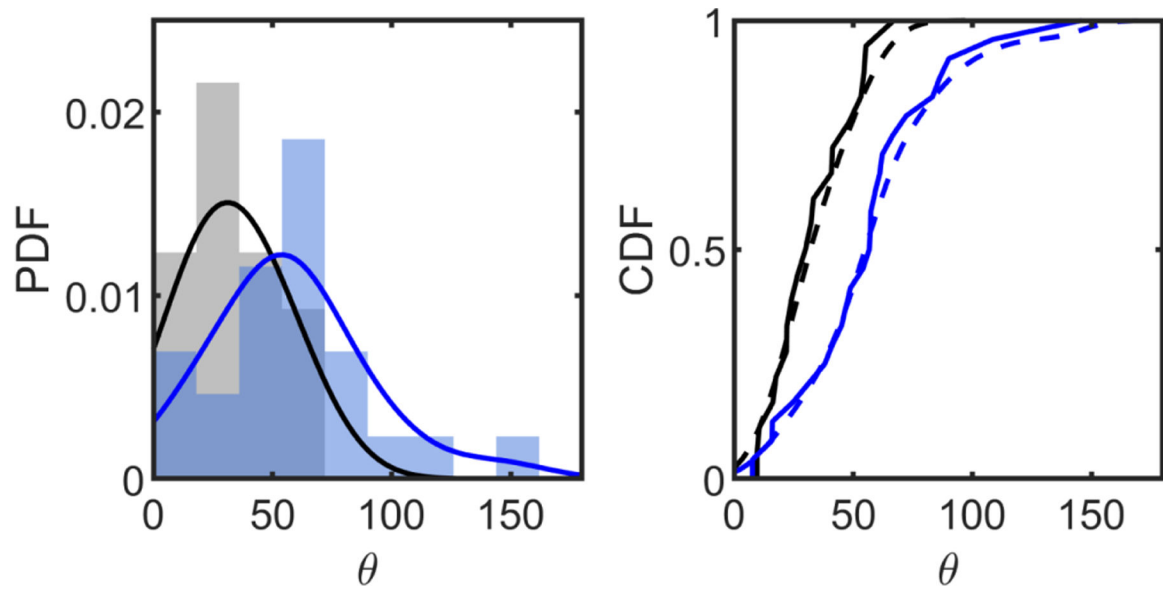
FIG. 8.

Polar angle distribution for *ace2* and *rsr1* yeast cells. Left: probability distribution functions for polar angle for *ace2* (gray) and *ace2 rsr1* (blue). Solid lines are kernel-smoothed estimates of the density distribution. Right: CDFs of the two distributions. Solid lines are the empirical CDF; dashed lines are kernel-smoothed estimates. The two distributions are statistically different via a *t* test with $t = 2.94$, $p = 0.005$, and $df = 40$.
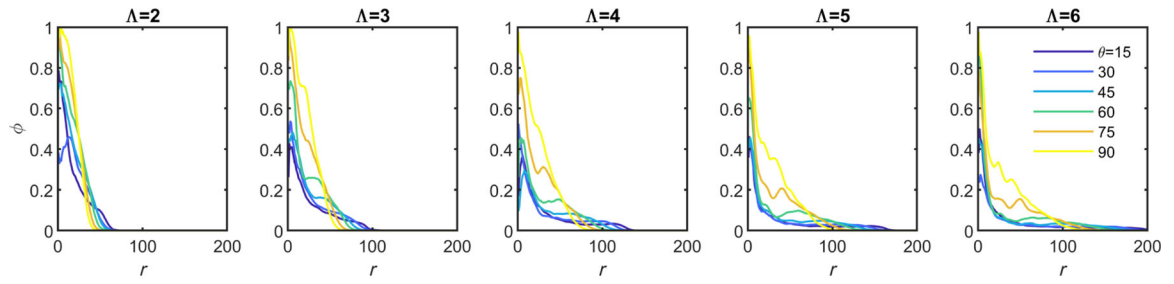
FIG. 9.

Density maps of example clusters after six branching events, showing the density ϕ changing with distance from the center of the tree r in simulation units.
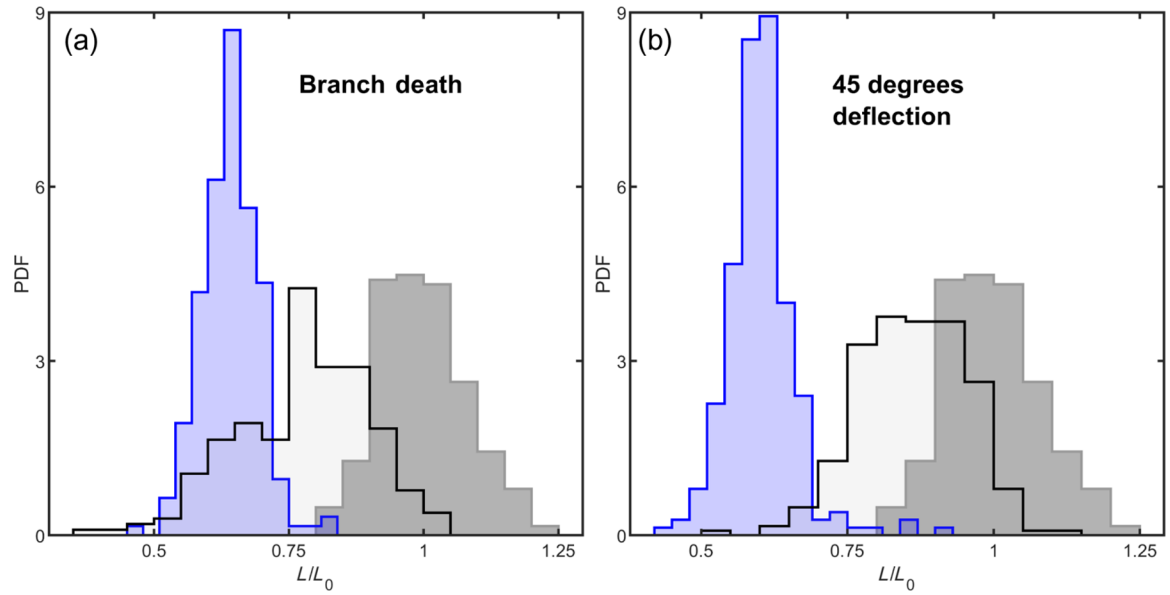
FIG. 10.

Growing and pushing simulations for situations where, instead of deflecting 90° when encountering an existing branch, hyphal tips either die (left) or deflect by 45° (right). In gray is the distribution of closest center of mass distance when trying to push trees as close as possible. Blue is the distribution of center of masses after growth. The black line is the result of taking the grown trees and trying to repush them together.
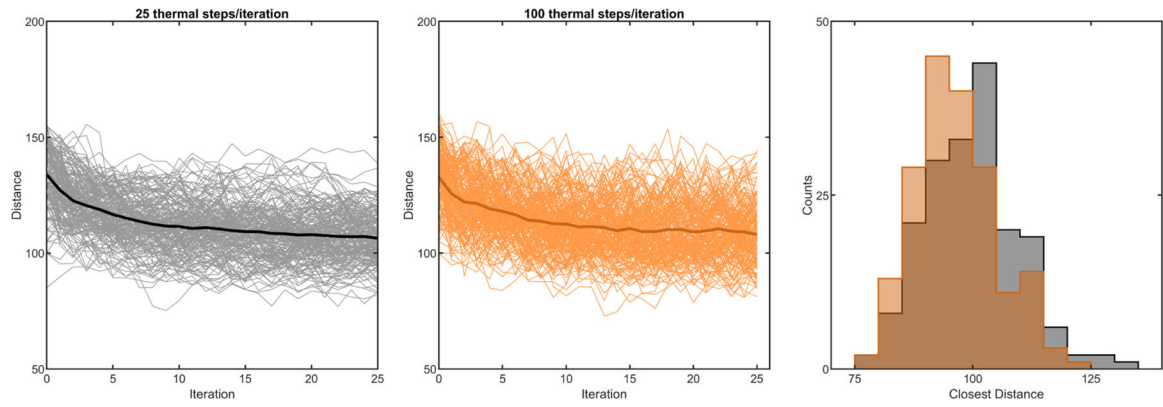
FIG. 11.

Testing the algorithm for pushing or agitating trees as close as possible. Left: center of mass distance vs iteration number for 300 different simulated trajectories, where each iteration cycles (a) 25 random "kicks" combining a random translation and random rotation and then (b) an external force that pushes the trees together until they collide. The dark line is the mean of the different simulations. Middle: the same plot where there are 100 random kicks instead of 25 random kicks per iteration. Right: the distribution of closest center of mass distance across the 300 simulations for both cases.